

CFD modeling the diffusional losses of nanocluster-sized particles and condensing vapors in 90° bends of circular tubes

Miska Olin^{*}, Miikka Dal Maso

Aerosol Physics Laboratory, Physics Unit, Tampere University, 33014, Tampere, Finland

ARTICLE INFO

Keywords:

Diffusion
Bend
Nanocluster
Sulfuric acid

ABSTRACT

Particle and vapor measurements typically include sampling tubing causing sampling losses therein. Correcting measured concentrations from the sampling losses using the calculated penetration efficiencies of straight tubes is a satisfactory approximation if sub-micrometer particles are of interest. However, in addition to inertial impaction of larger particles, bends in the tubing can cause a significant increase in diffusional losses of particles smaller than 5 nm or of condensing vapor, such as sulfuric acid. Here, the effects of 90° bends with various curvatures (dimensionless curvatures of 1.3 – 67) on the diffusional losses in a wide range of Reynolds (25 – 10000) and Schmidt (0.48 – 1400) numbers were simulated using computational fluid dynamics. The results were parametrized to output the functions for the penetration efficiencies of a bend.

1. Introduction

Interpreting nanoparticle measurement data usually involves correcting the measured concentrations from diffusional losses in the sampling lines. The most famous function for calculating the penetration efficiency of particles in a straight circular tube (p_s) was derived by Gormley and Kennedy (1948) (hereafter denoted as the G&K function). It assumes a laminar flow with a fully developed parabolic flow profile at the tube inlet. However, many realistic applications include parts that disturb the flow profile, e.g., bends, elbows, and expanders.

Large particles (micrometer-sized) are prone to deposit onto walls via inertial impaction due to flow disturbances. The smaller particles, instead, follow the fluid streamlines well, expressed with a small Stokes number (St). When nanometer-sized particles are of interest, flow disturbances can usually be neglected in diffusional loss calculations due to low effect of inertial impaction for these low-St particles. Therefore, e.g., in a case of a bent tube, the G&K function provides a relatively satisfactory approximation for small particles even though it is derived for straight tubes.

Secondary flow patterns are induced in smooth bends of tubes and cause Dean vortices that cause transport perpendicular to the tube flow axis (Dean, 1927). Fig. 1 presents a secondary flow profile of a bend with the dimensionless curvature ($\mathcal{R} = r/R$ where r is the radius of curvature and R is the tube inner radius) of 1.3 and the Reynolds number ($Re = 2\bar{v}R/\nu$ where \bar{v} is the average velocity and ν is the kinematic viscosity) of 4900. The strength of the secondary flow is determined by the Dean number ($De = Re/\sqrt{\mathcal{R}}$). A bend also directs the majority of the flow to travel near the outer curve wall instead of the centerline of the tube.

Whereas the penetration efficiency due to diffusion of particles smaller than 1 μm in particle diameter (D_p) can be estimated well with the G&K function also for bent tubes, diffusive penetration of very small particles ($D_p < 20$ nm), however, exhibit effects from

^{*} Corresponding author.

E-mail address: miska.olin@tuni.fi (M. Olin).

bends that are not captured by the G&K function (Frederix et al., 2017; Ghaffarpasand et al., 2012; Kwak et al., 2020; Lin et al., 2015; Wang et al., 2002; Yin et al., 2015; Yook & Pui, 2006). Wang et al. (2002) measured the effect of a single 90° bend with \mathcal{R} of 6.2 on the penetration efficiency of particles with D_p between 5 and

12 nm and obtained the reduction of penetration from 1 % \pm 3 % (10 nm) to 4 % \pm 4 % (5 nm) compared to a straight tube with the same length. The uncertainties were relatively high because the differences of the particle concentrations between the systems were small when the tubing contained only a single bend. Nevertheless, a negative correlation between D_p and the reduction of penetration can be seen in their measurement data, which is also the case in the experiments of Kwak et al. (2020), where the penetration efficiencies of 3 – 10 nm particles decreased \sim 10 % in a sharp-bent tube compared to a straight tube. For a single bend, the effect is relatively low for these particle sizes, but can be remarkable if the whole system contains multiple bends. Lin et al. (2015) constructed a parametrization for the penetration efficiency of particles larger than 8 nm in tubes containing a bent part (p_b). Kwak et al. (2020) constructed the parametrization for particle sizes of 3 – 50 nm and Re of 200 – 1500 in a sharp-bent tube. Recent introductions of instruments capable in measuring particles even down to 1 nm (e.g., Vanhanen et al., 2011) have invoked a lot of attention on sub-3 nm particles. The effect of 90° bends on the diffusional losses, especially for sub-3 nm particles, have not extensively been studied before. The penetration efficiency of a bend (p), defined as p_b/p_s , is a function of Re, De and the Schmidt number ($Sc = \nu/\mathcal{D}$ where \mathcal{D} is the diffusion coefficient) (Wang et al., 2002). Hence, p does not represent the penetration efficiency of a bent tube as a whole system; instead, it represents a multiplier with which the straight-tube penetration efficiency, p_s , is multiplied to obtain the penetration efficiency of the whole system, p_b . Extensive examination of p experimentally would require several tubes bent with different curvatures, several flow rates, and several generated particle size distributions having different particle sizes together with precise concentration measurement and high repeatability.

Because the G&K function is based on the Péclet number ($Pe = Sc \cdot Re$), it has been analogous to use it—or another functions for turbulent flow—also when calculating p_s for condensing vapors (e.g., Olin et al., 2020; Tröstl et al., 2016). One of the most widely studied condensing vapor is sulfuric acid (H_2SO_4), having a similar Sc to a particle with D_p of 0.8 nm. Because the effect of a bend increases with decreasing Sc, H_2SO_4 and sub-3 nm particles can exhibit significant effects from bends.

The purpose of this study is to simulate the diffusional losses of particles or vapors in 90° bends via computational fluid dynamics (CFD) modeling. A modeling approach was selected due to challenges in measuring very small particles or H_2SO_4 with the required level of precision. The outcome of the study is a parametrization for p in a wide range of Re, Sc, and \mathcal{R} . The chosen range for Re includes both laminar and turbulent flows. The range for Sc is aimed to correspond to particle sizes from $D_p = 23$ nm down to 0.4 nm or to condensing vapors down to the size of a water molecule, even though the smallest ones are presently not needed in penetration calculations. Particles larger than 23 nm were not considered because the effects of bends on the diffusional losses begin to be negligible already with particles larger than \sim 10 nm.

2. Modeling

2.1. CFD model

A commercially available CFD solver, ANSYS Fluent 19.0, was used to simulate the diffusional losses in tube flows. ANSYS Fluent uses a finite volume method to solve partial differential equations governing the motion of viscous fluids. Simulating laminar flow requires mass and momentum conservation equations to be solved. Additionally, a transport equation for a species mass fraction, Y , is solved when transport of gaseous or particulate matter is simulated. For a steady-state case, this is in the form of

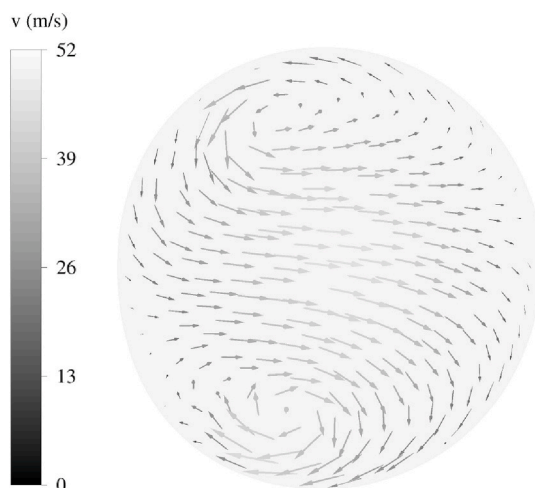


Fig. 1. Secondary flow velocity (v) profile inside a leftward bend with $\mathcal{R} = 1.3$ and $Re = 4900$, i.e. $De = 4300$.

$$\frac{\partial(\rho Y)}{\partial t} = -\nabla \cdot (\rho Y \mathbf{v}) + \nabla \cdot (\rho \mathcal{D} \nabla Y) = 0 \quad (1)$$

where t is time, ρ is the fluid density, and \mathbf{v} is the velocity vector. The last term in Eq. (1) represents diffusion of the species, and the diffusional losses are simulated by setting Y on the wall surfaces to zero. \mathcal{D} for a particle of a specific D_p is expressed as Stokes-Einstein relation (Hinds, 1999)

$$\mathcal{D} = \frac{k_B T C_c}{3\pi\mu D_p}, \quad (2)$$

where k_B is the Boltzmann constant, T is temperature, C_c is the slip correction coefficient (Kim et al., 2005), and μ is the dynamic viscosity.

In turbulent flow simulations, a Reynolds stress tensor appears in time-averaged momentum conservation equations. To maintain a reasonable computing time, the Reynolds stress tensor is typically modeled using available turbulence models, instead of simulating the chaotic and time-dependent flow field in a full form. In this study, the SST- $k-\omega$ turbulence model was selected because it was found to be the optimal one of several available turbulence models in simulating a turbulent flow in a 180° bend (Güden, 2014) and because the diffusional losses in a straight tube simulated using the SST- $k-\omega$ model corresponded best with a straight-tube penetration efficiency for turbulent flow by Brockmann (2005), which is based on Re, Sc, and Pe.

The SST- $k-\omega$ turbulence model was used with optional preferences of low-Re corrections and curvature effects because the range of Re was relatively low for turbulence modeling, from 2000 to 10000, and because the effects of curvatures are of interest in this study. The turbulent Schmidt number (Sc_t) determines the magnitude of the effect of the turbulent viscosity on the turbulent diffusion, which enhances the total diffusion over the laminar diffusion and is frequently the dominating one in turbulent flows. The optimal value for Sc_t for various flow types is typically in the range of 0.2 – 1.3 (Tominaga & Stathopoulos, 2007). In this study, Fluent's default value of 0.7 was reduced to 0.45 in order to make the simulated diffusional losses in a straight tube correspond to the values of the function of p_s in turbulent flow by Brockmann (2005).

2.2. Computational mesh

The geometry and the computational mesh for a bend with $\mathcal{R} = 6.7$ is shown in Fig. 2. The mesh is 3-dimensional but only the mesh on the tube wall is shown for clarity. In addition to the bent parts, the geometries contain extensions of $L = 2R$ at the both ends of the bend; the extension at the outlet end, especially, is beneficial in the simulations because, otherwise, there would be back flow at the outlet in some cases, causing difficulties in calculating the flow rate of the studied matter. Additionally, geometries of straight tubes with lengths equal to straightened bend geometries—considering the extensions too—were constructed. The geometries had $2R = 3$ mm but the results are applicable in all diameters due to normalizing of the flow rates via Re.

The meshes had the density of approximately 30 computational cells within the length of $2R$. Hence, the total number of the cells are 0.2 – 3.7 million, depending on r due to its effect on the total length and volume of the geometry. To ensure that the mesh density was sufficient, the results of a simulation with the original mesh were compared to a simulation with an 8-fold mesh density, which had a relative effect of less than 2% on the penetration efficiency. Additionally, the penetration efficiencies in the meshes of the straight tubes were compared to p_s predicted with the G&K function (Fig. 3, left panel). The differences were well below 1%, with the exception of cases with low Pe because of a drawback of the G&K function which makes it not to suit very well in the low-Pe regime due to higher axial diffusion, which was neglected in its derivation. Nevertheless, possible minor uncertainties arising from the nonidealities of the meshes or from the uncertainties of the turbulence model were minimized by calculating p with p_b/p_s where p_s is obtained from

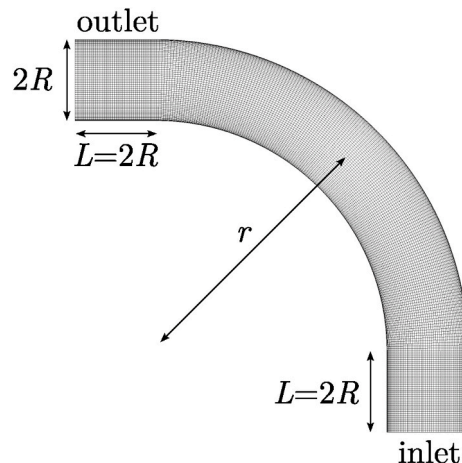


Fig. 2. The schematics of the geometry and the computational mesh for a bend with $\mathcal{R} = 6.7$.

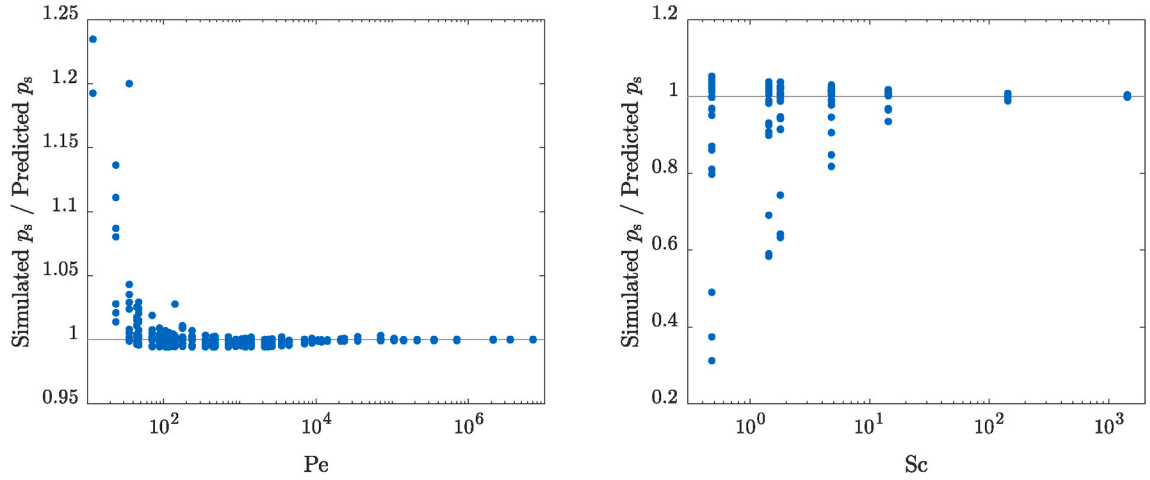


Fig. 3. The simulated penetration efficiencies of straight tubes divided by the predicted ones (Brockmann, 2005; Gormley & Kennedy, 1948) as a function of (left panel) Pe in the laminar cases and (right panel) Sc in the turbulent cases.

simulations with the straight tubes rather than from the G&K function. In this manner, the drawback of its low suitability in the low-Pe regime is overcome too.

The used turbulent model, SST- $k-\omega$, behaves well with all values of the dimensionless wall distance in turbulent modeling (y^+). In these simulations, it was in the range of 1 – 15. The simulated results were compared to simulations with the mesh refined to the y^+ values of 1 – 5 and of ~ 1 ; the relative differences between these simulations were only about 0.1 %, implying that the grid density on the walls was appropriate. Comparing the simulated p_s to the ones predicted by the function of Brockmann (2005) (Fig. 3, right panel), differences of several tens of percents are observed with $Sc < 10$, corresponding to $D_p < 2$ nm. The largest discrepancies are from the cases with the longest tubes, in which $p_s < 0.3$, i.e., within a slightly impractical range. The discrepancies with small values of Sc imply that the empirical function by Brockmann (2005) does not hold for particle sizes this low, which is reasonable because the function has been developed before the introduction of particle counters measuring sub-3 nm particles and is thus best applicable in the range of $Sc \gg 1$. When Sc becomes lower than unity, molecular diffusion becomes such strong that the turbulent diffusion does not play the major role in the overall diffusion process anymore, resulting in different behaviors with low and high values of Sc.

2.3. Input parameters

Simulations were performed in the parameter ranges shown in Table 1. The ranges differ between the laminar and turbulent cases because of different ranges of Re. The ranges of Re were chosen to cover also the transitional regime between laminar and turbulent flows.

The velocity profiles at the inlets were assumed to be fully developed profiles, as is the assumption in the derivation of the G&K function too. For the laminar cases, those are of the form of the analytically solved parabolic velocity profile,

$$v(R^*) = 2\bar{v} \left[1 - \left(\frac{R^*}{R} \right)^2 \right] \quad (3)$$

Table 1

The ranges of parameters within which the simulations were performed. The top three parameters denote the defining parameters of the simulations and the bottom four ones the parameters which are derived from the defining parameters. ^L denotes the laminar cases and ^T the turbulent cases.

Parameter	Range
Re	25 – 4900 ^L / 2000 – 10000 ^T
Sc	0.48 – 1400
\mathcal{R}	1.3 – 67 ^L / 2 – 67 ^T
\mathcal{D} at 298 K (m ² /s)	1.1 · 10 ⁻⁸ – 3.2 · 10 ⁻⁵
D_p at 298 K (nm)	0.4 – 23
De	6 – 1900 ^L / 240 – 7200 ^T
Pe	12 – 7.1 · 10 ⁶ ^L / 940 – 1.5 · 10 ⁷ ^T

where R' is the distance from the tube centerline axis. For the turbulent cases, a commonly used empirical velocity profile, the power-law profile for $Re < 10000$,

$$v(R') = 1.32\bar{v} \left(1 - \frac{R'}{R}\right)^{1/5}, \quad (4)$$

was used. However, velocity profiles are, in practice, never fully developed unless there is enough straight tube before the inlet; the required length is determined by the velocity entrance length (L_v), which is calculated, e.g., by $L_v = 0.1Re \cdot R$ for laminar flow (Durst et al., 2005) and $L_v = 8.8Re^{1/6} \cdot R$ for turbulent flow. In this study, L_v are in the range of $2.5R - 490R$ in the laminar cases and $31R - 41R$ in the turbulent cases. These are usually satisfied in realistic applications because some straight tube usually precedes a bend.

The concentration (or mass fraction) profiles of the studied matter at the inlet are also assumed to be fully developed. The profile for laminar flow derived by Alonso et al. (2016),

$$Y(R') = Y(0) \cdot \left[1 - \frac{18}{11} \left(\frac{R'}{R}\right)^2 + \frac{9}{11} \left(\frac{R'}{R}\right)^4 - \frac{2}{11} \left(\frac{R'}{R}\right)^6\right], \quad (5)$$

was used for both the laminar and the turbulent cases. Although it is not intended for turbulent flow, it was selected to approximate the profile also for the turbulent cases because, in reality, the profile would depend in a complex manner on the value of Sc in turbulent flow. As in the case of L_v , the development of the concentration profiles is determined by the concentration entrance length (L_Y), which is calculated, e.g., by $L_Y = 0.1Re \cdot Sc \cdot R$ for laminar flow. In the laminar cases of this study, L_Y is in the range between $1.2R$ (water molecule) and $7.1 \cdot 10^5 R$ (23 nm particle). Hence, for condensing vapor molecules, the assumption of the fully developed concentration profiles is usually satisfactory but not for larger particles. Therefore, the laminar cases were simulated also with constant concentration profiles, representing the another extreme end, the undeveloped profiles. In turbulent flow, mixing is much stronger; therefore, the lengths are much shorter also for larger particles and the developed profile holds better.

In addition to the choices between the developed or constant velocity and concentration profiles, another uncertainty arises from the effects of bends—or other disturbances—in the downstream direction. E.g., if multiple bends with the connecting tubes shorter than L_v exist, the velocity profiles at the inlets of the subsequent bends are different, depending also on the physical arrangement of the bends. Hence, the penetration efficiencies in the bends and in the connecting tubes cannot be simply calculated with p and p_s . Wang et al. (2002) measured the penetration efficiencies of the systems with four 90° bends in different configurations and obtained differing results compared to the penetration efficiency of a single bend raised to the power of four. However, these complex effects of multiple disturbances were omitted in this simulation study in order to maintain simplicity.

2.4. Model validation

The CFD model was validated by comparing the simulation results against the measurement results of Wang et al. (2002) and Kwak et al. (2020). The experiment of Wang et al. (2002) with a single smoothly-bent tube was performed with $Re = 250$ and was selected as a validation experiment. The experiments of Kwak et al. (2020) with a sharp-bent tube performed with $Re = 200$ and $Re = 1500$ were also selected as validation experiments.

Instead of the extensions with lengths of $L = 2R$ as in the geometry presented in Fig. 2, these validation experiments were simulated with the extensions of the real lengths as in the experiments. Additionally, the boundary conditions of the velocity and concentration at the inlets were set constants rather than the fully developed forms. The sharp-bent tube used in the experiments of Kwak et al. (2020) is

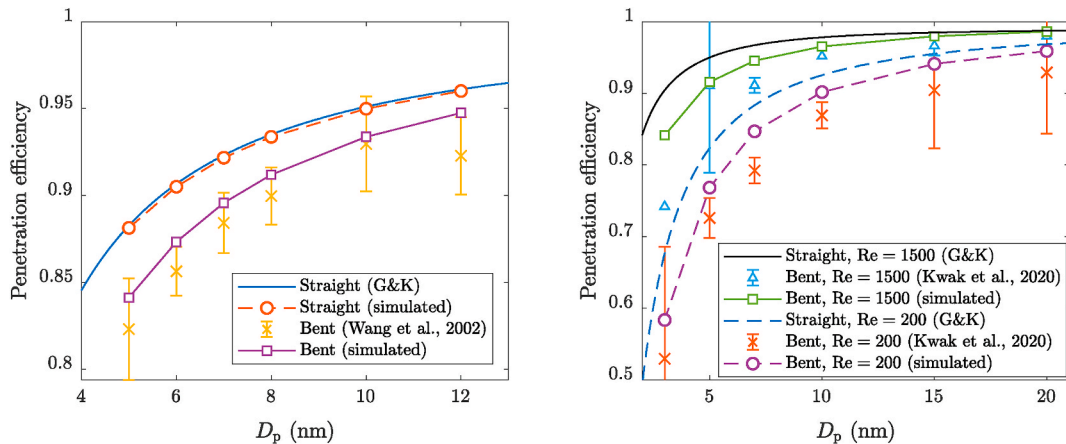


Fig. 4. The measured (Kwak et al., 2020; Wang et al., 2002) and simulated penetration efficiencies of the systems with bends and straight tubes of equal lengths of the validation experiments as functions of D_p . The left panel represents the validation experiment measured by Wang et al. (2002) and the right panel represents the validation experiments measured by Kwak et al. (2020).

of a slightly different geometry compared to the geometries of this study. It corresponds to $\mathcal{R} = 1$ at the inner curve and $\mathcal{R} = 0.5$ at the outer curve; however, the simulation was performed with $\mathcal{R} = 1.1$ because the used model restricts that $\mathcal{R} > 1$.

Due to the lack of the experimental data in turbulent regime, no specific validation simulation was performed for that. Instead, the validity of the turbulent model relies on the value of Sc_t adjusted according to the empirical function of p_s in turbulent flow by Brockmann (2005).

3. Results and discussion

3.1. Validation results

The penetration efficiencies in the systems related to validation experiments are presented in Fig. 4.

The left panel shows the penetration efficiencies of the bend (p_b) measured by Wang et al. (2002) together with the simulated results. The simulated penetration efficiencies of the straight tube of an equal length (p_s) together with the G&K function are also shown. It can be observed that in both the experiment and the simulation, penetration is reduced when the tube is bent. The effect of the bend according to the simulations is slightly weaker compared to the experiments but still agrees when the experimental uncertainties are taken into account.

The right panel shows p_b measured by Kwak et al. (2020) together with the simulation results. The effect of the bend compared to the G&K function can be observed in the experiments and in the simulations. However, the simulated effect seems to be somewhat weaker than the measured effect even though the experimental uncertainties are taken into account. This discrepancy may be related to the fact that the simulation geometry differs slightly from the real experiment.

3.2. Main results and parametrizations

The penetration efficiencies of the systems with a bend (p_b) or a straight tube (p_s) were obtained from the simulations as the ratios of the mass flow rates of the studied matter at the outlet to the mass flow rates at the inlet. The penetration efficiencies of the bends, defined as $p = p_b/p_s$, as functions of \mathcal{R} for different example values of Re and Sc in the laminar flow cases are presented in Fig. 5. It can be observed that the effect of bends increase with decreasing Sc , i.e. with increasing \mathcal{D} or decreasing size of the particle or the vapor molecule. It can also be observed that, somewhat unexpectedly, p decreases with increasing \mathcal{R} in most cases, which is discussed later.

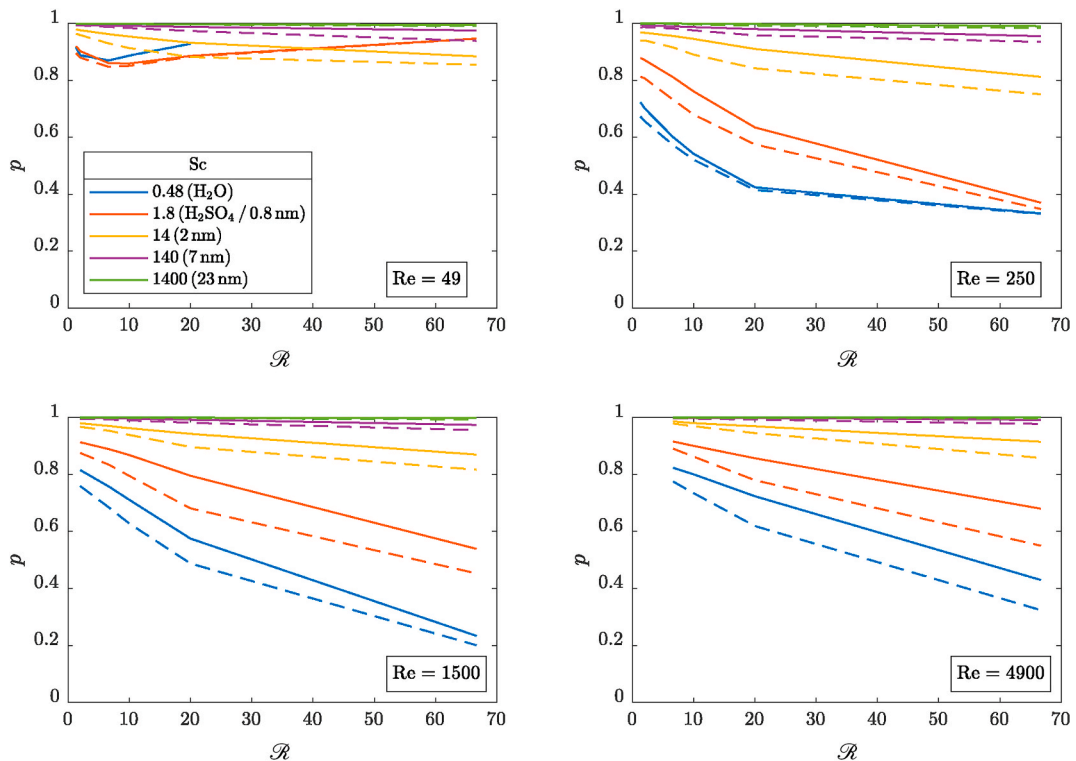


Fig. 5. The penetration efficiencies of bends, p , as functions of \mathcal{R} for different values of Re and Sc in the laminar flow cases. Solid lines represent the cases with the constant concentration profile at the inlet and dashed lines the cases with the developed concentration profile. Different colors represent different values of Sc ; corresponding example vapors and particle diameters are shown in the legend. (For interpretation of the references to color in this figure legend, the reader is referred to the Web version of this article.)

Fig. 6 presents example results of the laminar flow cases as functions of Sc and Re . The left panel presenting p as a function of Sc for different example values of Re indicates that the effect of a bend with $\mathcal{R} = 6.7$ becomes considerable with the values of Sc below 100 or D_p below 5 nm. The results of Wang et al. (2002) are also shown, which lie near the same level as the simulated results of this study, particularly when the uncertainties of the experiments are taken into consideration. Instead of $\mathcal{R} = 6.7$, the experiments by Wang et al. (2002) were performed with $\mathcal{R} = 6.2$; nevertheless, the values are close enough to compare these results in this plot. The right panel presenting p as a function of Re for different example values of \mathcal{R} indicates that the effects of bends are, in most cases, considerable if the diffusional losses of H_2SO_4 vapor (or 0.8 nm particles) are of interest. When Re is low (roughly below 40), the effects of bends become minor and the effect of \mathcal{R} is different than for higher values of Re . At a specific value of Re (60 – 500, depending on \mathcal{R}), the effects of bends begin to decrease with increasing Re . While lower values of Re seem to have higher penetration efficiencies, the penetration efficiencies for the bends as whole systems, $p_b = p \cdot p_s$, are, however, much lower.

Fig. 7 illustrates how the effect of a bend becomes negligible if Re is low enough. With low values of Re , the parabolic velocity profile is sustained well in the bend because the velocities are low compared to the dimensions of the bend. Instead, with high values of Re , the velocities are such high that the flow impacts with the outer curve wall of the bend. When the flow is impacted with the wall, particles and condensing vapors are also pushed toward the wall, causing increased diffusional losses.

The reason for the decreasing p with increasing \mathcal{R} is because when the matter is pushed toward the wall, it remains longer near the outer curve wall due to increased total length of the bend. Nevertheless, when Re increases high enough, the time spent inside the bend becomes shorter and the effect of the bend becomes weaker, resulting in higher p . This also results in minimums in the p vs. Re curves in the right panel of Fig. 6. Additionally, when \mathcal{R} increases high enough—eventually approaching infinity (denoting a straight tube)—the effect of a bend begins to weaken. This can be observed in the case of $Re = 49$ and $Sc \leq 1.8$ in Fig. 5; in the other cases, the values of \mathcal{R} are not high enough for this observation. For higher values of Re , the required \mathcal{R} is higher due to higher flow rates leading to stronger impact of the flows with the outer curve walls. The required values of \mathcal{R} with which p begins to increase with increasing \mathcal{R} are remarkably high in some cases. This implies that, e.g., flexible hoses can have significant effects on the diffusional losses of very small particles or condensing vapors because hoses are rarely in a straight form. Additionally, the radii of curvature of flexible hoses can alter during a measurement if the hoses are touched or moved, causing the penetration efficiencies to alter too.

As the magnitude of p comprises of the combined effect of Re and \mathcal{R} , their effects are partly combined into the effect of De . Fig. 8 presents the penetration efficiencies of bends as functions of De for different values of Sc and Re with the developed concentration profile at the inlets. Basically, p increases with increasing De in the laminar cases but is still dependent on the value of Re . More precisely, the value of Sc alters the behavior of p as a function of De . With low enough values of Re , p decreases with increasing De with very low values of De but begins to increase with higher values. The existence of this behavior is controlled by the value of Sc .

Example results from the turbulent cases are also shown in Fig. 8. The values of p are higher with turbulent flows compared to laminar flows, which results from the chaotic and strongly mixing nature of turbulent flow. Because in turbulent flow, the flow field is chaotic anyway, bends do not further alter the flow field in very high extent. Additionally, the effect of bends pushing the matter toward the curve walls is competed by the strongly mixing nature of turbulent flow, which flattens the concentration profiles across the tube profiles. While turbulent flows seem to have higher penetration efficiencies than laminar flows, the overall penetration efficiencies are, however, lower because the values of p_s are usually lower in the case of turbulent flows compared to laminar flows. In the turbulent cases, the effects of De and Re are relatively minor but the effect of Sc is notable. Because $Re = 2000$ is possibly not in the turbulent regime, the applicability of the function of p_s in turbulent flow may be reduced, causing a differing trend in p vs. De plot

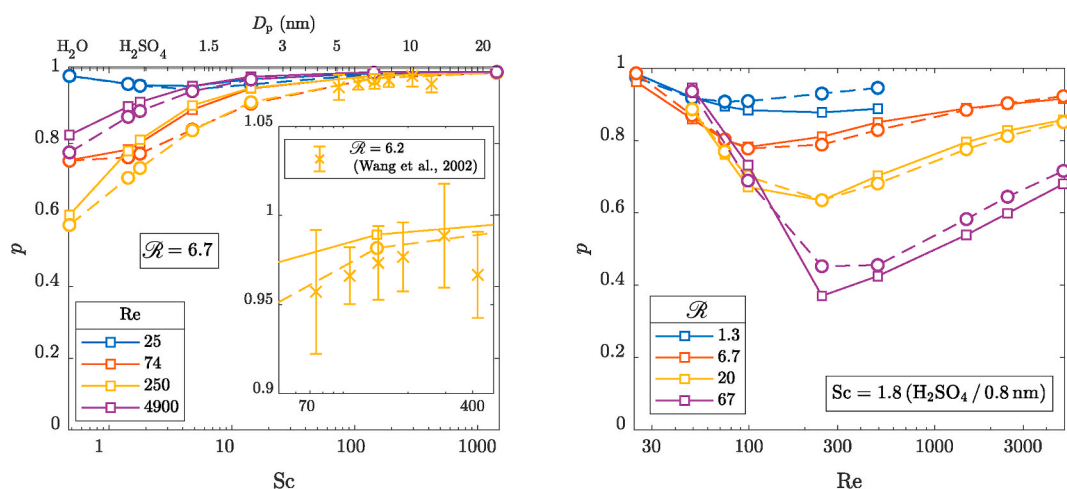


Fig. 6. The penetration efficiencies of bends, p , as functions of (left panel) Sc or D_p and (right panel) Re in the laminar flow cases. The left panel represents a bend with $\mathcal{R} = 6.7$ for different values of Re . The insert zooms the case with $Re = 250$ together with the measurement data by Wang et al. (2002) with $\mathcal{R} = 6.2$. The right panel represents $Sc = 1.8$, corresponding a H_2SO_4 molecule or a 0.8 nm-sized particle, for different values of \mathcal{R} . Solid lines with squares represent the cases with the constant concentration profile at the inlet and dashed lines with circles the cases with the developed concentration profile.

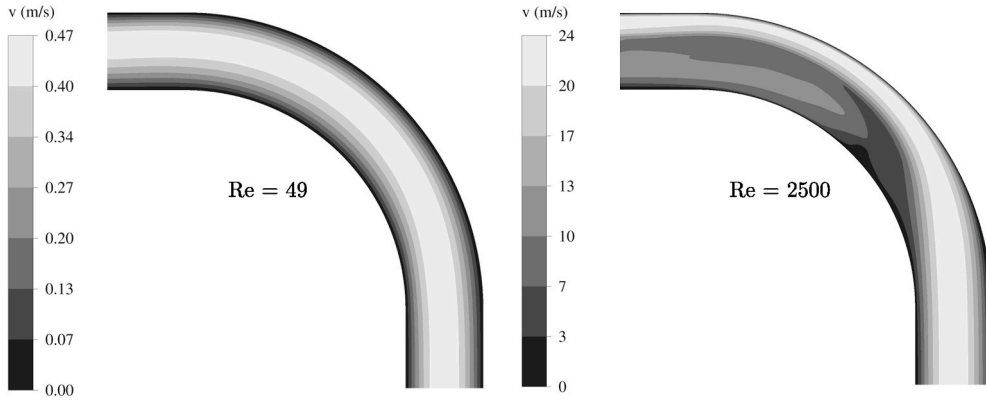


Fig. 7. Velocity contour plot in a bend with $\mathcal{R} = 6.7$ and different values of Re showing that the parabolic velocity profile is sustained well when the flow rate is low but that the flow impacts with the outer curve wall of the bend when the flow rate is high.

compared to the higher values of Re.

Fully experimental parametrizations for p as functions of Re, Sc, and \mathcal{R} were constructed to cover the ranges of them as given in Table 1. For laminar flow with the developed concentration profile at the inlet, p can be calculated with the equation

$$p = 1 - 0.076 \cdot \ln^2(0.08 \text{ Re}) \cdot \exp \left[- \frac{\ln^2(0.009 \text{ Re}^{1.35} \text{ Sc}^{0.54} \mathcal{R}^{-0.5})}{\ln^2(0.9 \text{ Re}^{0.43})} \right], \quad (6)$$

which is also presented graphically in Fig. 8. For laminar flow with the constant concentration profile at the inlet, p can be calculated with the equation

$$p = 1 - 0.085 \cdot \ln^2(0.07 \text{ Re}) \cdot \exp \left[- \frac{\ln^2(0.016 \text{ Re}^{1.24} \text{ Sc}^{0.54} \mathcal{R}^{-0.5})}{\ln^2(0.82 \text{ Re}^{0.38})} \right]. \quad (7)$$

For the turbulent flow cases, p can be calculated with the equation

$$p = 1 - \ln^3 \left[1.775 \cdot \left(\frac{\mathcal{R}}{\text{Re Sc}^2} \right)^{0.024} \right]. \quad (8)$$

The uncertainties of the parametrizations are at the level of 0.02. The penetration efficiency of a system containing a bend, p_b , can be obtained by multiplying these equations with the corresponding p_s function; however, a minor error arises from the G&K function in the low-Pe regime. Even a higher error arises from the function by Brockmann (2005) when both Sc is lower than ~ 10 and the tube is such long that $p_s < 0.3$.

4. Conclusions

The penetrations efficiencies of the systems with single 90° bends, p_b , with different curvatures were simulated with a commercial CFD solver, ANSYS Fluent. The obtained penetration efficiencies were compared with the penetration efficiencies simulated with straight tubes having the total lengths equal to the bent tubes, p_s . These penetration efficiencies of the systems provided the penetration efficiencies of the bends, $p = p_b/p_s$.

Estimating the penetration efficiency in a system containing single or multiple bends and straight tubes connecting them can be done as follows. First, the system is divided into parts of straight tubes and straight tubes with bent parts. Secondly, the penetration efficiencies of the divisions (for both types) are calculated with the straight-tube penetration efficiencies, such as with the G&K function for laminar flow or with the function by Brockmann (2005) for turbulent flow. Next, the penetration efficiencies of the bends, p , are calculated with Eqs. (6) and (7), and/or (8). Finally, all the calculated penetration efficiencies are multiplied together to obtain the penetration efficiency of the whole system. To obtain the penetration efficiency for a particle mass concentration, e.g., in a case of a polydisperse particle size distribution, particle size-dependent p needs to be calculated separately for all particle sizes.

The effects of multiple disturbances, e.g., the velocity profiles in the downstream direction of a bend, were not taken into consideration in this study. Instead, these results output p for cases with the developed parabolic velocity profile at the inlet of a bend, both for laminar and turbulent flow. The concentration profiles at the inlets are, nevertheless, considered both as the fully developed profiles and as the constant profiles for laminar flow. The decision of choosing a suitable parametrization for laminar flow between Eqs. (6) and (7) can be made by comparing the length in the upstream direction of a bend to L_Y with the governing values of Re, Sc, and \mathcal{R} . It is worthwhile to note that when Eq. (6) is chosen, the G&K function needs to be used in the concentration-developed form, i.e. the tube lengths are artificially increased over L_Y , rather than in the original form, because the original form assumes the constant concentration profile at the inlet.

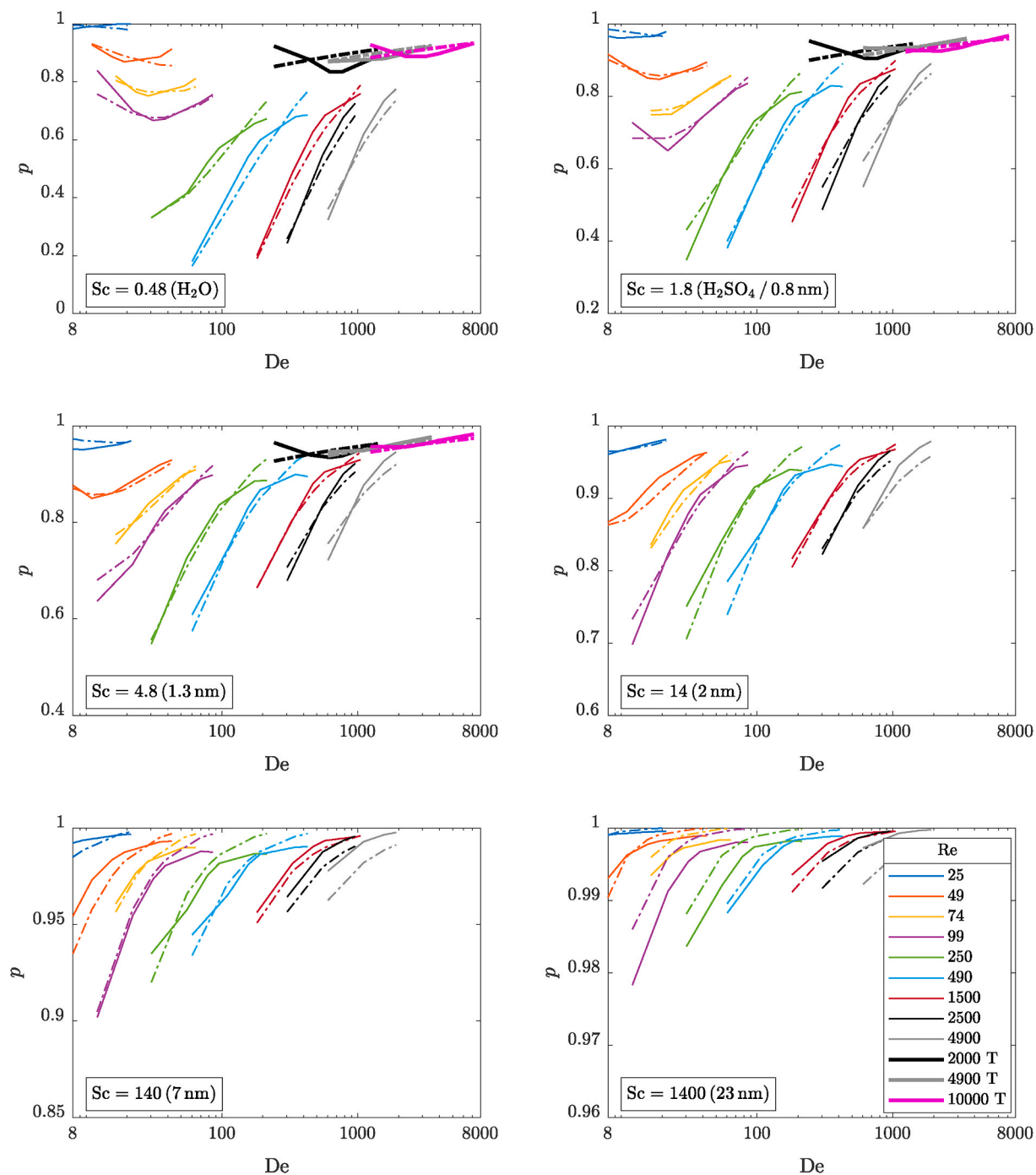


Fig. 8. The penetration efficiencies of bends as a function of De for different values of Sc and Re with the developed concentration profile at the inlets. Different colors represent different values of Re ; the ones marked with T denote turbulent flow (shown only in the first three panels for clarity). Solid lines represent the simulation results and dash-dotted lines the parametrizations. (For interpretation of the references to color in this figure legend, the reader is referred to the Web version of this article.)

Declaration of competing interest

M. D. is an Associate Editor for the Journal of Aerosol Science. The handling editor for this submission was Chris Hogan (Editor-in-Chief), and M. D. was blinded from the peer-review process.

Acknowledgements

This work was supported by the Academy of Finland through the Condenz project [grant number 326437].

References

- Alonso, M., Carsí, M., & Huang, C.-H. (2016). Using the fully developed concentration profile to determine particle penetration in a laminar flow tube. *Journal of Aerosol Science*, *97*, 34–37. <https://doi.org/10.1016/j.jaerosci.2016.04.002>.
- Brockmann, J. E. (2005). Sampling and transport of aerosols. In P. A. Baron, & K. Willeke (Eds.), *Aerosol measurement: Principles, techniques, and applications* (2nd ed., pp. 143–195). Hoboken, USA: John Wiley & Sons.
- Dean, W. (1927). XVI. Note on the motion of fluid in a curved pipe. *Philosophical Magazine*, *4*, 208–223. <https://doi.org/10.1080/14786440708564324>.
- Durst, F., Ray, S., Ünsal, B., & Bayoumi, O. A. (2005). The development lengths of laminar pipe and channel flows. *Journal of Fluids Engineering*, *127*, 1154–1160. <https://doi.org/10.1115/1.2063088>.
- Frederix, E., Kuczaj, A., Nordlund, M., Veldman, A., & Geurts, B. (2017). Eulerian modeling of inertial and diffusional aerosol deposition in bent pipes. *Computers & Fluids*, *159*, 217–231. <https://doi.org/10.1016/j.compfluid.2017.09.018>.
- Ghaffarpasand, O., Drewnick, F., Hosseinibalam, F., Gallavardin, S., Fachinger, J., Hassanzadeh, S., & Borrmann, S. (2012). Penetration efficiency of nanometer-sized aerosol particles in tubes under turbulent flow conditions. *Journal of Aerosol Science*, *50*, 11–25. <https://doi.org/10.1016/j.jaerosci.2012.03.002>.
- Gormley, P. G., & Kennedy, M. (1948). Diffusion from a stream flowing through a cylindrical tube. *P. Roy. Irish Acad. A*, *52*, 163–169. <https://doi.org/10.2307/20488498>.
- Güden, Y. (2014). *Analysis and control of complex flows in U-bends using computational fluid dynamics*. Master's thesis. Middle East Technical University.
- Hinds, W. C. (1999). *Aerosol technology: Properties, behavior, and measurement of airborne particles* (2nd ed.). Hoboken, USA: John Wiley & Sons.
- Kim, J. H., Mulholland, G. W., Kukuck, S. R., & Pui, D. Y. H. (2005). Slip correction measurements of certified PSL nanoparticles using a nanometer differential mobility analyzer (Nano-DMA) for Knudsen number from 0.5 to 83. *J. Res. Natl. Inst. Stand. Technol.*, *110*, 31–54. <https://doi.org/10.6028/jres.110.005>.
- Kwak, D.-B., Kim, S. C., Lee, H., & Pui, D. Y. (2020). Experimental study of nanoparticle transport and penetration efficiency on a sharp-bent tube (elbow connection). *International Journal of Heat and Mass Transfer*, *155*, 119816. <https://doi.org/10.1016/j.ijheatmasstransfer.2020.119816>.
- Lin, J.-Z., Yin, Z.-Q., Lin, P.-F., Yu, M.-Z., & Ku, X.-K. (2015). Distribution and penetration efficiency of nanoparticles between 8–550nm in pipe bends under laminar and turbulent flow conditions. *International Journal of Heat and Mass Transfer*, *85*, 61–70. <https://doi.org/10.1016/j.ijheatmasstransfer.2015.01.033>.
- Olin, M., Kuuluvainen, H., Aurela, M., Kalliokoski, J., Kuittinen, N., Isotalo, M., Timonen, H. J., Niemi, J. V., Rönkkö, T., & Dal Maso, M. (2020). Traffic-originated nanocluster emission exceeds H₂SO₄-driven photochemical new particle formation in an urban area. *Atmospheric Chemistry and Physics*, *20*, 1–13. <https://doi.org/10.5194/acp-20-1-2020>.
- Tominaga, Y., & Stathopoulos, T. (2007). Turbulent schmidt numbers for cfd analysis with various types of flowfield. *Atmospheric Environment*, *41*, 8091–8099. <https://doi.org/10.1016/j.atmosenv.2007.06.054>.
- Tröstl, J., Chuang, W. K., Gordon, H., Heinritzi, M., Yan, C., Molteni, U., Ahlm, L., Frege, C., Bianchi, F., Wagner, R., Simon, M., Lehtipalo, K., Williamson, C., Craven, J. S., Duplissy, J., Adamov, A., Almeida, J., Bernhammer, A.-K., Breitenlechner, M., ... Baltensperger, U. (2016). The role of low-volatility organic compounds in initial particle growth in the atmosphere. *Nature*, *533*, 527–531. <https://doi.org/10.1038/nature18271>.
- Vanhanen, J., Mikkilä, J., Lehtipalo, K., Sipilä, M., Manninen, H. E., Siivola, E., Petäjä, T., & Kulmala, M. (2011). Particle size magnifier for nano-CN detection. *Aerosol Science & Technology*, *45*, 533–542. <https://doi.org/10.1080/02786826.2010.547889>.
- Wang, J., Flagan, R. C., & Seinfeld, J. H. (2002). Diffusional losses in particle sampling systems containing bends and elbows. *Journal of Aerosol Science*, *33*, 843–857. [https://doi.org/10.1016/S0021-8502\(02\)00042-3](https://doi.org/10.1016/S0021-8502(02)00042-3).
- Yin, Z., Lin, J., & Lou, M. (2015). Penetration efficiency of nanoparticles in a bend of circular cross-section. *Journal of Hydrodynamics*, *27*, 93–98. [https://doi.org/10.1016/S1001-6058\(15\)60460-7](https://doi.org/10.1016/S1001-6058(15)60460-7).
- Yook, S.-J., & Pui, D. Y. H. (2006). Experimental study of nanoparticle penetration efficiency through coils of circular cross-sections. *Aerosol Science & Technology*, *40*, 456–462. <https://doi.org/10.1080/02786820600660895>.